Optik 124 (2013) 3314–3318

Contents lists available at SciVerse ScienceDirect

Optik

journal homepage: www.elsevier.de/ijleo

Internal inspection of semi-transparent objects by digital holographic micro-tomography

F.A. Monroy-Ramirez[a,*], A.E. Dolinko[b], J. Garcia-Sucerquia[c]

[a] Department of Physics, Universidad Nacional de Colombia, Bogotá, Colombia
[b] Applied Electromagnetism Group, Physics Department, FCEN, Universidad de Buenos Aires – IFIBA (CONICET), Ciudad Universitaria, Pabellón I, Buenos Aires, Argentina
[c] Universidad Nacional de Colombia-Sede Medellin, School of Physics, A.A: 3840, Medellin 050034, Colombia

ARTICLE INFO

Article history:
Received 22 June 2012
Accepted 15 October 2012

Keywords:
Digital holography microscopy
Axial tomography
Digital holographic micro-tomography
Non-destructive evaluation

ABSTRACT

The combined use of digital holographic microscopy and computer tomography, here named digital holographic micro-tomography, is used to examine the interior of transparent channels. The proposed method is used to identify internal obstacles inside of transparent troughs having slightly different refractive index. The method is based in the acquisition of a set of digital holograms of the specimen whereas it is axially rotated from 0° to 180°. The phase differences retrieved from the obtained holograms are the inputs to a computerised axial tomography procedure. The technique has been numerically modelled in order to find the optimal tomographic conditions and also to realise the minimum difference of refractive index the method could detect. The obtained results show the feasibility of the proposed method for the non-destructive evaluation of transparent micro-objects.

1. Introduction

The present great step forward in the scientific development leads to high competitive pace in the field of high-tech technologies. The development of very affordable digital cameras with spatial resolution of the order of 100 p/mm or better has brought the possibility of replacing the use of photographic films in diverse environments. This development in combination with powerful computing systems merge ideally in a relatively new field named digital holography (DH) [1]. From DH many branches have appeared in scene, being one of the most attractive digital holographic microscopy (DHM) [2]. DHM has the unique feature of providing quantitative phase information of microscopic objects, surpassing other microscopy methods as phase contrast- or differential interference contrast-microscopy [3]. DHM can be applied to the study of either opaque or transparent specimens [4]. Essentially, DHM is an interferometric technique that determines the optical phase difference (OPD) between two waves travelling via the arms of an optical setup. As in any interferometry test, the OPD gathers the differences of lengths of the arms and refractive index as seen by the travelling waves. If the object under study has micrometric dimensions, the OPD $\approx \int 2\pi/\lambda_0 \Delta n(x, y, z)\, dz$ and therefore the OPD provides information of the difference of refractive index [5]. By taking advantage of this property provided by DHM, a clever combination of DHM and computerised tomography (CT) has been proposed [6] for studying the internal distribution of the refractive index in the interior of a cell. In the marriage, a regular scheme of CT [7] is applied to a set of maps that are obtained for different orientations of the specimen under study. From those tomographs the full and detailed internal distribution of the refractive index of a cell can be obtained; the same approach can be extended to others fields of the research of technology. In this paper we name the merged utilization of DHM and CT, digital holographic micro-tomography (DHMT). DHMT can be used to identify regions of different refractive index inside the specimen, as objects stuck in the interior of transparent objects. Those objects, that may be an obstacle in a trough, vein or any other micro-channel, could be invisible to regular microscopy techniques, because they have very similar refractive index to the walls of the trough. Since DHMT uses phase maps obtained from DHM, the CT of those maps can lead to a morphological, and even quantitative, identification of the objects in the interior of the channel.

In this paper, we apply DHMT as a tool to characterise obstacles located in the interior of transparent micro-channels. The method is fully numerically modelled with an approach based on 3D hypermatrices. The computer model is implemented to find the optimal experimental conditions for the tomographic reconstruction procedure and to estimate the minimum refractive index difference that is detectable by the method. The simulation shows that an obstacle having a difference as small as 0.01 in the refractive index is detectable by the method, which is in good agreement with the obtained experimental results. In Sections 2 and 3, we briefly

* Corresponding author. Tel.: +57 1 3165000x13045/13046/13026.
E-mail address: famonroyr@unal.edu.co (F.A. Monroy-Ramirez).

0030-4026/$ – see front matter © 2012 Elsevier GmbH. All rights reserved.
http://dx.doi.org/10.1016/j.ijleo.2012.10.062

introduce the basis of DHM and CT, respectively, to present DHMT in Section 4. The modelling procedure is described in Section 5 and the experimental results are shown in Section 6.

2. Digital holography microscopy

Digital holographic microscopy (DHM) provides quantitative measurement of the optical path difference via interferometric experiments. This approach enables to investigate transparent samples with diffraction-limited transverse resolution and sub-wavelength axial sensitivity [8]. For simplicity, the specimen is illuminated by means of a plane wave and the light that emerges from it is directed to an objective lens. The resulting wavefront, called *the object wave* (O), is combined onto a CCD sensor with a second light beam named *the reference wave* (R). The combination of both beams, gives rise to an intensity distribution called *digital hologram*.

The intensity of the produced digital hologram I_H can be expressed as [9]

$$I_H(x,y) = |R|^2 + |O|^2 + R^*O + RO^*, \tag{1}$$

where O^* and R^* refer to the complex conjugate of O and R respectively and (x,y) indicates the spatial coordinates on the hologram plane.

The terms R^*O and RO^* in (1) correspond to both, the real and virtual reconstructed images respectively, which are spatially separated for off-axis geometries [9]. The term $|R|^2 + |O|^2$ corresponds to the zero diffraction order or DC term. This DC term has a deleterious effect on the recovered images because it looks like a very bright square area that conceals any other information due to it sets a value of intensity too high for the largest number of the dynamic range of visualization. Fortunately, there are many approaches to get rid of the DC term and the entire nuisance associated with it [10]. Those procedures can be understood as a pre-processing of the digital hologram which leads to $\tilde{I}_H(x,y) = RO^* + R^*O$. In order to recover the object information having no information of the DC term, the pre-processed digital hologram $\tilde{I}_H(x,y)$ is multiplied times the reference wave R. Usually R is a plane unitary wavefront and, therefore $\tilde{\tilde{I}}_H(x,y) = \tilde{I}_H(x,y)R = O^* + O$. After this digital manipulation the recorded hologram at the CCD camera only contains information about the object wave and its complex conjugate. Since DHM uses the versatility of the numerical propagation, we can compute the object wavefront at any plane a distance d away from the CCD plane. Such propagation in the Fresnel–Fraunhofer approximation is given by [1]:

$$\psi(\xi,\eta,d) = A\exp\left[\frac{i\pi}{\lambda d}(\xi^2+\eta^2)\right]\int\int \tilde{\tilde{I}}_H(x,y)\exp \times \left[\frac{i\pi}{\lambda d}(x^2+y^2)\right]\exp\left[\frac{i2\pi}{\lambda d}(x\xi+y\eta)\right]dxdy \tag{2}$$

where $A = 1/(i\lambda d)\exp(i2\pi d/\lambda)$ is a complex constant, λ is the light wavelength, d is the propagation distance and (ξ,η) are the coordinates at the reconstruction plane. The computational implementation of (2) resorts on the fast Fourier transform (FFT) algorithm and on the sampled version of $\tilde{\tilde{I}}_H(x,y)$:

$$\psi(m,n,d) = A\exp\left[\frac{i\pi}{\lambda d}(m^2\Delta\xi^2+n^2\Delta\eta^2)\right]FFT \times \left\{\tilde{\tilde{I}}_H(k,l)\exp\left[\frac{i\pi}{\lambda d}(k^2\Delta x^2+l^2\Delta y^2)\right]\right\}, \tag{3}$$

where k, l, m, n are integers satisfying the condition $-M/2 \le k, l, m, n \le M/2$, with M the number of elements of the sensor; the CCD has dimensions $\Delta x, \Delta y$; $\Delta\xi, \Delta\eta$ are the values of the intervals of sampling on the reconstruction plane (ξ, η). Then, the intensity $I(m,n,d)$ and the phase $\phi(m,n,d)$ corresponding to the reconstructed optical field $\psi(m,n,d)$ can be evaluated as:

$$I(m,n,d) = \mathrm{Re}[\psi(m,n,d)]^2 + \mathrm{Im}[\psi(m,n,d)]^2 \tag{4}$$

$$\phi(m,n,d) = \arctan\frac{\mathrm{Im}[\psi(m,n,d)]}{\mathrm{Re}[\psi(m,n,d)]}, \tag{5}$$

where Re and Im stand for the real and imaginary parts of complex field and the function arctan accounts for the signs of the $\mathrm{Im}[\psi(m,n,d)]$ and $\mathrm{Re}[\psi(m,n,d)]$ in the computation of the inverse tangent function.

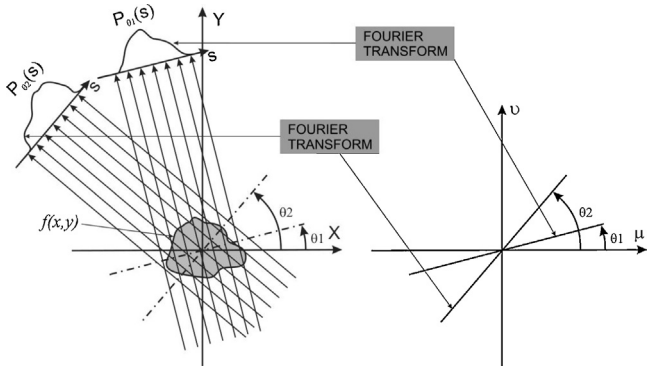

Fig. 1. Illustration of the principles of computerised tomography. At left the projection of the object for different angles is described by the Radon transform of the function $f(x,y)$. At right the Fourier slice theorem is illustrated.

3. Computerised tomography

Computerised tomography (CT) is the technique of reconstructing an object image from its projections. The simplest CT method is the non-diffractive approach, in which the light travelling within the specimen travels following straight paths. Under this approach, the light should not be strongly diffracted by the test object.

Hence, for plane wave illumination all the light rays are parallel. As illustrated in Fig. 1 (at left) each light ray gathers information of the object as it travels. The cumulate information on each ray contributes to generate a projection of the object on a recording screen. For plane wave illumination each projection is produced by all the parallel rays that propagate through the object. For each ray $\mathbf{s}$ the projected information of the object $f(x,y)$ is represented by the Radon transform of the function $f(x,y)$ [7]:

$$P_\theta(\mathbf{s}) = \int_{-\infty}^{+\infty}\int_{-\infty}^{+\infty} f(x,y)\delta(x\cos\theta + y\sin\theta - \mathbf{s})\,dxdy. \tag{6}$$

where P_θ is the one-dimensional projection of the function $f(x,y)$ as the object is illuminated at angle θ and δ is the delta function. In Fig. 1, at left is illustrated the Radon transform for two angles of illumination $\theta 1$ and $\theta 2$. The projections $P_{\theta 1}(\mathbf{s})$ and $P_{\theta 2}(\mathbf{s})$ correspond to the object information cumulate on each ray denoted by the set of points along each line $\mathbf{s} = x\cos\theta + y\sin\theta$. Each of the multiple projections of the object for the different rotation angles θi, with i ranging from 1° to $180^\circ/N$ and N the number of projections, is related with the object information at that angle via the Fourier slice theorem [7]: *The Fourier transform of a parallel projection of an image f(x, y) taken at angle θi gives a slice of the two-dimensional transform, F(μ,υ), subtending an angle θi with the μ-axis*. In other words, the Fourier transform of $P_{\theta i}(\mathbf{s})$ gives the values of $F(\mu,\upsilon)$ along line that subtends and angle θi with the μ-axis; as illustrated on the right side of Fig. 1.

According to the general principles of CT, the tomographic information of an object is obtained by: (i) taking N projections of the object, (ii) Fourier transforming each projection, (iii) summing

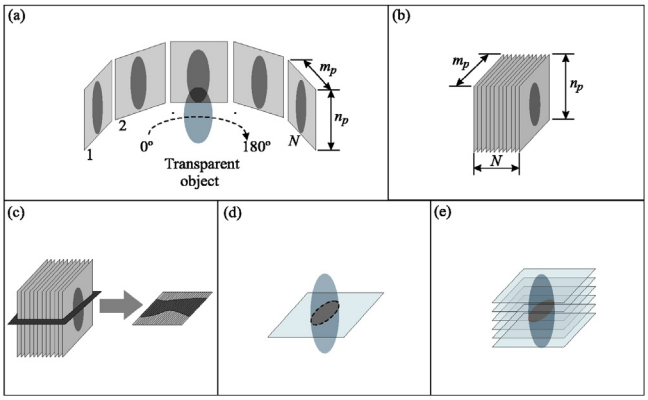

Fig. 2. Illustration of DHMT: (a) generation of tomographic projections; (b) ordering the projections in the hyper-matrix; (c) extraction of a set of 1D projections; (d) tomographic slice; (e) three-dimensional composition of the reconstructed object.

all the Fourier transforms, and (iv) inverse Fourier transforming the obtained sum. To perform the (iii) step there are different approaches that lead to almost identical results. In this work we have used the standard *inverse Radon transform*, which uses a filtered back-projection algorithm of the Fourier slice theorem.

In order to be able to apply the non-diffractive CT approach in our experiments, we have minimised the deviation of the light travelling through the sample by immersing it in an index matching liquid. Therefore, the closer the refractive index of the index matching liquid to that of the trough, the better the results.

4. Digital holographic micro-tomography

The combined use of DHM and CT leads to a technique that we name digital holographic micro-tomography (DHMT). In this technique, we use the capability of DHM of producing quantitative phase maps of transparent or transparent objects via the digital holograms. Those phase maps can be related with the refractive index of the object through the OPD $\approx \int 2\pi/\lambda_0 \Delta n(x, y, z)\, dz$, and therefore slight difference of refractive index $\Delta n(x,y,z)$ can be detected. If N phase images are properly produced those can be the necessary images by CT to work. Hence, N digital holograms are recorded while the object under study is rotated. Those holograms are processed and N phase maps of the object are obtained. These phase maps constitute the input for the axial tomography procedure.

As illustrated in Fig. 2, for DHMT to work a set of transmission microscopy digital holograms of a transparent specimen is acquired whereas the object is rotated from 0° to 180° with a step angle θi (see panel (a)). If for instance $N = 100$, it means that one digital microscopy hologram is taken every $\theta i = 1.8°$; each hologram is composed by $n_p \times m_p$ pixels. The recorded holograms are reconstructed at the object plane and the phase maps (Eq. (5)) computed. For most of the applications, those phase maps need to be unwrapped. In this work the unwrapping process has been done with the algorithm proposed and implement by Ruiz et al. [14]. Once the phase maps are unwrapped, the N phase images are stacked in a cubic matrix or hyper-matrix with dimensions $n_p \times m_p \times N$; we name this matrix S_p (Fig. 2(b)). Then, from the stack S_p we take a slice of $m_p \times N$ elements for each n_i (i from 1 to n_p) position and the *inverse Radon transform* [7] is applied to such slice (Fig. 2(c)). According to the Fourier slice theorem, the result of the result of the inverse Radon transform corresponds to a slice of the object at the corresponding height n_i (Fig. 2(d)). The process is repeated for n_i and the results placed in a second hyper-matrix called R_b that contains the three-dimensional distribution of relative refractive index corresponding to the specimen (Fig. 2(e)).

5. DHMT modelling

The quality of the tomographic reconstruction depends on several parameters such as the number of digital holograms involved, the step-angle θi between the acquisition of successive holograms and the coincidence between the vertical axis of the imaging area and the rotation axis of the specimen. In order to calibrate the experimental set-up and to find the optimum parameters, a simulation of the tomographic procedure was implemented. The same modelling tool has also been used to estimate the minimum refractive index difference that DHMT can detect.

The simulation generates a set of phase maps similar to those obtained from the digital holograms of the sample recorded at angles from 0° to 180°. The three-dimensional transparent object to be simulated is generated inside a 3D hyper-matrix called R_m which represents the refractive index distribution of the object. This hyper-matrix has a size corresponding to the width, depth and height of the volume containing the transparent object to be simulated. Every cell in R_m is initialised with a value equal to the refractive index of the medium surrounding the object. This in this case corresponds to the index matching liquid to be used. Then, the object itself is generated following two different procedures depending on its symmetry. In the case of an object with prismatic symmetry, the matrix is filled by reading a set of digital images or bitmaps representing different slices of the object. The grey levels of the pixels of each bitmap are associated to the refractive index of the corresponding slice, following the method for interpreting the bitmaps described in Refs. [11,12]. Therefore, the size of the three dimensions of the R_m matrix will be defined according to a scale factor, having units in μm/pixel, relating the physical dimensions of the object to be simulated and the size of its representation in the digital images. If the object is a sphere, the corresponding region is generated by the matrix cells satisfying the following condition:

$$\frac{(i-i_c)^2}{R^2} + \frac{(j-j_c)^2}{R^2} + \frac{(k-k_c)^2}{R^2} < 1. \quad (7)$$

The matrix indices i, j and k in Eq. (7) correspond to the physical coordinates x, y and z, respectively. The indices i_c, j_c, and k_c are the coordinates of the hyper-matrix cell corresponding to the sphere centre. The value R determines the radius of sphere. The cells contained in this region are set equal to the desired refractive index for the generated sphere.

Once the 3D hyper-matrix containing the three-dimensional distribution of refractive index of the transparent object is generated, the set of 2D radon projections at different angles is obtained. This is made by sweeping the 3D matrix along the k index corresponding to the z direction. Firstly, the 1D Radon projections of each slice of the 3D hyper-matrix are evaluated. The obtained values correspond to the optical path traversed by the light along the cross section of the evaluated slice. Then, the 2D Radon projection at each angle is computed by combining all the 1D projections generated at different values of the k coordinate for the corresponding angle, i.e. following the inverse reconstruction procedure described in Section 3. The obtained 2D image corresponds to the tomographic projection for each angle. Since one obtains experimentally the optical phase from the recorded holograms, the image obtained from the Radon transform, which corresponds to the optical path difference is multiplied by $2\pi/\lambda$. In this way, the obtained images correspond to the simulated unwrapped optical phase which would be provided by holograms obtained from the simulated 3D sample for each rotation angle. The simulation is completed when the set of synthetic phase maps for a given simulated 3D transparent object is obtained for the whole set of angles from 0° to 180°. The number of phase maps will depend on the used step-angle θi.

In order to test the tomographic procedure, we have modelled a specimen with similar size and refractive index to that tested

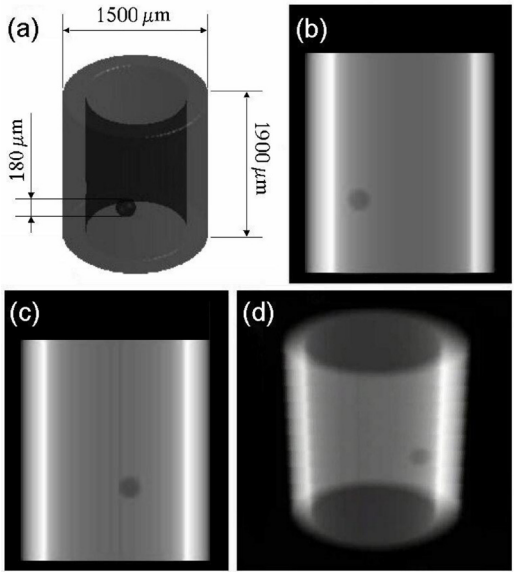

Fig. 3. DHMT modelling. (a) The 3D-rendering of the modelled object. The obstacle inside the trough has a absolute difference of refractive index of 0.01 with respect to the index matching liquid. (b and c) The simulated optical phase obtained for two different angles of the modelled object. The tomographic reconstruction obtained from the 100 projections is shown in (d).

experimentally. For that purpose, a micro-channel with a refractive index of 1.5 was simulated. As obstacle within the trough, we have included a glass micro-sphere of 180 μm in diameter with a refractive index of 1.46. The object is immersed in a liquid with a 1.47 refractive index (corresponding to glycerine). Fig. 3(a) shows the modelled object for which the difference of refractive index between the sphere and the surrounding liquid is 0.01. Fig. 3(b) and (c) shows different projections that are obtained with the simulation for two particular angles. The 3D tomographic reconstruction generated with the whole set of simulated phase map projections is shown in Fig. 3(d). In this figure it is clear that the method can recover the information of the obstacle inside the channel as the difference of the refractive index is 0.1. It should be noticed that the detectability will depend upon the size of the obstacle and the sensitivity of the phase measurement, determined by the dynamic range of the digital camera used to record the holograms.

6. Experimental results

6.1. Experimental setup

The experimental set-up we have used is depicted in Fig. 4. It consists in a modified Mach–Zehnder interferometer. A He–Ne laser (l = 632.8 nm, 35 mW) is used for illumination. The variable attenuators (A) allow for controlling the light intensity that enters into the interferometer. The filtered and expanded beam, produced by the spatial filter (SF) and the lens (C), is divided by the beam splitter (BS) into the reference and object beams. The sample (RS) is a glass capillary and an objective lens 4×/0.10 (MO_o) is used to magnify the hologram in order to use a digital camera as recording screen. An objective lens 3.2×/0.10 (MO_r) is added in the reference beam for wavefront compensation [13]. The object and reference beams (waves) are combined by means of a beam splitter (BS) that directs them towards a CCD sensor (Camera Sensor, Lumenera of 1280 × 1024 square pixels of 6.5 μm of pixel size), where both beams interfere, generating the digital hologram. Since the object and reference beams have different curvatures, the registered interference pattern is composed by non-periodic circular fringes whose variation in space frequency is determined by the lateral

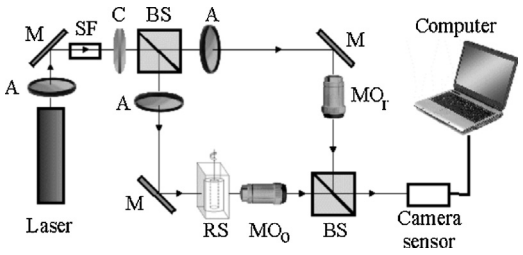

Fig. 4. Schematic diagram of the experimental setup: mirrors (M), spatial filter (SF), collimating lens (C), beam splitter (BS), attenuators (A), sample (RS), objective lens in the reference beam path (MO_r), objective lens in the object beam path (MO_o).

magnification of the objective lenses MO_r and MO_o. The beam splitter (BS) in front of the CCD sensor is placed on a rotation stage that allows controlling the incidence angle between the object and reference beams on the sensor plane, assuring specific conditions for the off-axis geometry [10]. The sample is placed on a holder coupled to a stepper motor that allows a step-by-step rotation. The stepper motor is connected to an electronic interface that permits controlling its position by means of a personal computer. To achieve the index matching required for applying non-diffractive CT, the sample is submerged in a chamber filled with a liquid with a refractive index close to the walls of the capillary.

6.2. Results from processed holograms

In the experiment, a glass micro-capillary with a refractive index n_{sample} = 1.5, outer radius of 1500 ± 10 μm and inner radius of 1100 ± 10 μm was used. In order to evaluate the best index matching that minimises the refractive effects at the interface of the sample such that the non-diffractive CT theory can be applied, two experiments were performed. In the first, the capillary was submerged in distilled water (n_{water} = 1.33), whereas in the second, the specimen was submerged in glycerine ($n_{glycerine}$ = 1.47). Fig. 5(a) and (b) shows the unwrapped phase of one hologram of the sequence acquired in the case of the capillary immersed in water and glycerine, respectively. Fig. 5(c) shows the corresponding tomographic reconstruction (top-down view) obtained using the axial tomography procedure of a slice of the capillary immersed in water, whereas Fig. 5(d) shows the equivalent image for the capillary immersed in glycerine. In those images we observe that the profile obtained in the case of glycerine (Fig. 5(d)) appears more clearly defined than in the case of the water (Fig. 5(c)). The information obtained from the tomographic images provides the relative refractive index between the absolute refractive index of the capillary and the medium where it is submerged. Using this information, the experimentally measured refractive index for the capillary was 1.5037 in the case of the glycerine (i.e. with a relative error of 0.24%) and 1.3639 in the case of the water (i.e. with a relative error of 9.07%). It can be noted that the error obtained in the case of the glycerine is very low in comparison with the error obtained in the case of the water. These results allow us to conclude that glycerine is the best choice for the index matching and therefore we used it for to test the capability of distinguishing obstacles inside the capillary.

In the following experiment a sphere of 180 μm in diameter and 1.458 refractive index was glued to the interior of the capillary. The latter was submerged in a chamber filled with glycerine and the DHMT procedure performed. Fig. 6(a) and (b) shows that the method can effectively distinguish obstacles inside transparent troughs. For the case of the present experiment, the method retrieves a refractive index of 1.445 and a diameter of 165 μm for the obstacle. The results support the idea of using DHMT as a tool to quantify obstructions by means of this non-invasive approach.

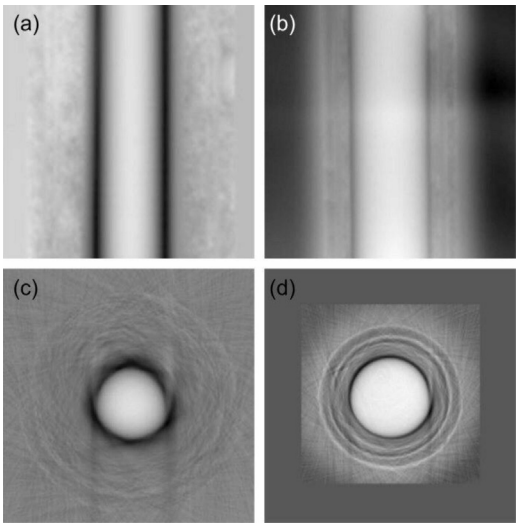

Fig. 5. Testing the index matching in DHMT. (a and b) Two unwrapped phase images as water and glycerine are used as index matching substances, respectively. (c) and (d) A slice of the tomographic (top-down view) for water and glycerine, respectively.

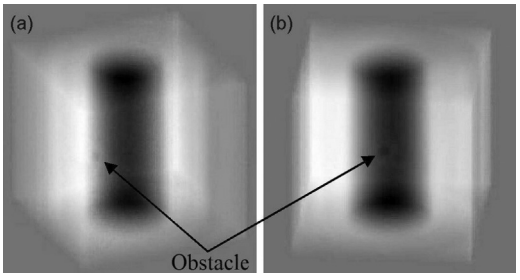

Fig. 6. Experimental obstacle observation with DHMT. (a) and (b) Two different views of the tomographically reconstructed capillary with an obstacle inside it.

7. Conclusions

We have presented a digital holography (DH) and computerised tomography (CT) combined method to produce tomography images of transparent objects. The method here named digital holographic micro-tomography (DHMT) has been utilized to characterise an obstacle present inside a transparent micro-channel. By means of computational modelling we have found that the method can distinguish objects with a minimum difference of refractive index about 0.01. The sensitivity of the method can be improved by increasing the dynamic range of the recording camera. As it can be expected, glycerine offers a better index matching than water as the object to be analysed with DHMT is made of glass. The proposed method shows promise as a non-invasive tool to characterise internal structures of transparent objects.

Acknowledgements

This work was partially supported by the Universidad Nacional de Colombia, Vicerrectoría de Investigación grants numbers 12932 and 12934. A.D. also wishes to thank the financial support provided by the Consejo Nacional de Investigaciones Científicas y Técnicas of Argentina (CONICET). The authors thank Gustavo E. Galizzi from Universidad Nacional de Rosario, Argentina, for providing the phase unwrapping algorithm.

References

[1] U. Schnars, W. Jueptner, Digital Holography: Digital Hologram Recording, Numerical Reconstruction, and Related Techniques, Springer-Verlag, Berlin, Heidelberg, 2005.
[2] C. Depeursinge, A.M. Marian, F. Montfort, T. Colomb, F. Charrière, J. Kühn, E. Cuche, Y. Emery, P. Marquet, Digital Holographic Microscopy (DHM) applied to Optical Metrology: a resolution enhanced imaging technology applied to inspection of microscopic devices with subwavelength resolution, in: W. Osten (Ed.), Fringe 2005: The 5th International Workshop on Automatic Processing of Fringe Patterns, Stuttgart, Germany, 2005.
[3] M. Pluta, Advanced Light Microscopy, vol. 1. Principles and Basic Properties, Elsevier, Amsterdam, 1988, 460 pp.
[4] E. Cuche, P. Marquet, C. Depeursinge, Simultaneous amplitude-contrast and quantitative phase-contrast microscopy by numerical reconstruction of Fresnel off-axis holograms, Appl. Opt. 38 (1999) 6994–7001.
[5] B. Rappaz, P. Marquet, E. Cuche, Y. Emery, C. Depeursinge, P. Magistretti, Measurement of the integral refractive index and dynamic cell morphometry of living cells with digital holographic microscopy, Opt. Express 13 (2005) 9361–9373.
[6] F. Charrière, A. Marian, F. Montfort, J. Kuehn, T. Colomb, E. Cuche, P. Marquet, C. Depeursinge, Cell refractive index tomography by digital holographic microscopy, Opt. Lett. 31 (2006) 178–180.
[7] A.C. Kak, M. Slaney, Principles of Computerized Tomographic Imaging, IEEE Press, New York, 1988.
[8] P. Marquet, B. Rappaz, P.J. Magistretti, E. Cuche, Y. Emery, T. Colomb, C. Depeursinge, Digital holographic microscopy: a noninvasive contrast imaging technique allowing quantitative visualization of living cells with subwavelength axial accuracy, Opt. Lett. 30 (5) (2005) 468–470.
[9] M. Liebling, T. Blu, M. Unser, Complex-wave retrieval from a single off-axis hologram, J. Opt. Soc. Am. A 21 (2004) 367–377.
[10] E. Cuche, P. Marquet, C. Depeursinge, Spatial filtering for zero-order and twin-image elimination in digital off-axis holography, Appl. Opt. 39 (2000) 4070–4075.
[11] A.E. Dolinko, Non-destructive visualization of defect borders in flawed plates inspected by thermal load, J. Phys. D: Appl. Phys. 41 (2008) 205503 (7 pp.).
[12] A.E. Dolinko, From Newton's second law to Huygens's principle: visualizing waves in a large array of masses joined by springs, Eur. J. Phys. 30 (2009) 1217–1228.
[13] M.K. Kim, Tomographic three-dimensional imaging of a biological specimen using wavelength scanning digital interference holography, Opt. Express 7 (2000) 305–310.
[14] P.D. Ruiz, G.H. Kaufmann, G.E. Galizzi, Unwrapping of digital speckle-pattern interferometry phase maps by use of a minimum L^0-norm algorithm, Appl. Opt. 37 (1998) 7632–7644.